Validation of Object-Induced MR Distortion Correction for Frameless Stereotactic Neurosurgery

David Dean,* *Member, IEEE,* Janardhan Kamath, *Member, IEEE,* Jeffrey L. Duerk, *Member, IEEE,* and Edward Ganz

***Abstract*—Spatial fidelity is a paramount issue in image guided neurosurgery. Until recently, three-dimensional computed tomography (3D CT) has been the primary modality because it provides fast volume capture with pixel level (1 mm) accuracy. While three-dimensional magnetic resonance (3D MR) images provide superior anatomic information, published image capture protocols are time consuming and result in scanner- and object-induced magnetic field inhomogeneities which raise inaccuracy above pixel size. Using available scanner calibration software, a volumetric algorithm to correct for object-based geometric distortion, and a Fast Low Angle SHot (FLASH) 3D MR-scan protocol, we were able to reduce mean CT to MR skin-adhesed fiducial marker registration error from 1.36 to 1.09 mm. After dropping the worst one or two of six fiducial markers, mean registration error dropped to 0.62 mm (subpixel accuracy). Three dimensional object-induced error maps present highest 3D MR spatial infidelity at the tissue interfaces (skin/air, scalp/skull) where frameless stereotactic fiducial markers are commonly applied. The algorithm produced similar results in two patient 3D MR-scans.**

***Index Terms*—Computed tomography (CT), craniofacial, fiducial, registration, susceptibility error.**

I. Introduction

IT IS PERHAPS a misnomer to refer to most stereotactic neurosurgical procedures as "image-guided." Use of preoperative three–dimensional (3-D) patient images rarely extends beyond planning and intraoperatively locating the craniotomy site and initial surgical tool positioning. However, these procedures have been shown to reduce craniotomy size and intracranial surgical traverse [1], [2]. Such "minimally invasive" neurosurgical procedures require high spatial fidelity between the patient's preoperative images and their intraoperatively localized anatomy. In order to insure the required accuracy, preoperative neurosurgical imaging is frequently done with CT. While CT is particularly useful in imaging bony structures, MR provides better definition of inhomogeneous soft tissue structures such as the brain.

Manuscript received March 30, 1998; revised June 25, 1998. The Associate Editor responsible for coordinating the review of this paper and recommending its publication was M. Viergever. *Asterisk indicates corresponding author.*

*D. Dean is with the Imaging Laboratory, Department of Neurological Surgery, Case Western Reserve University, 10900 Euclid Avenue, Cleveland, OH 44106 USA (e-mail: dxd35@po.cwru.edu).

J. Kamath was with the Department of Biomedical Engineering at Case Western Reserve University, Cleveland, OH 44106 USA. He is now with the CT Engineering Group at Picker International Inc., Highlands Heights, OH 44143 USA.

J. L. Duerk is with the Department of Radiology, Case Western Reserve University, Cleveland, OH 44106 USA.

E. Ganz is with the Department of Neurological Surgery, Case Western Reserve University, Cleveland, OH 44106 USA.

Publisher Item Identifier S 0278-0062(98)09092-2.

II. Scanner-Induced Geometric Distortion in MR

Scanner-induced MR image errors that affect stereotactic neurosurgical application accuracy [3]–[8], have been judged unacceptable for many procedures [3], [8]–[17]. Nonuniformities in the scanner's B_0 field (e.g., scanner imperfections, gradient field nonlinearities, shimming anomalies, and B_0 eddy currents) are known to geometrically distort resulting images.

Two improvements have reduced MR scanner-induced errors. First, better magnet technology has eliminated much distortion. Second, software now derives calibration maps of static magnetic field inhomogeneities *post-hoc* from MR-scans of machined phantoms [8], [17]–[19]. The effect of gradient field nonlinearity is significantly reduced with our three-dimensional magnetic resonance (3D MR) acquisition. We assume the remaining nonlinearities result in insignificant geometric distortion over the volume we image and need not be considered in our study [6], [22]. Not intended to represent human subjects, or correct for object-induced distortions, most gradient field calibration phantoms are standard geometric shapes with little material inhomogeneity.

III. Object-Induced Geometric Distortion in MR

The materials, especially fat and water, within a scanned neurosurgical patient's head have different susceptibility to small magnetic fields [19], [27]. This results in geometric image distortions referred to as "susceptibility errors" caused by "object-induced" inhomogeneities in the scanner's B_0 field. These errors are seen in all published MR image sequences [15]. Like other resonance offsets (e.g., chemical shift [26]), these distortions occur only along the read-out gradient direction [5], [19], [21], [22] and have been shown to be significantly large when a small read-out gradient and a large B_0 magnetic field are used [19], [23], [24].

Maximum distortion is expected at material interfaces with differing magnetic susceptibility [22], [25]. Not only do the MR-susceptibility of fat and water differ, but their proportions and distribution change over time in all patients due to aging, nutrition, health, and blood physiology. These temporal changes interact with changing patient pose within the read-out gradient in each new MR-scan. Since object-induced MR distortions are unique for every MR-scan session, this type of error is likely to be difficult to correct from prescan calibration data alone.

IV. Correction of Object-Induced MR Dstortion

Two methods have been used in attempts to correct object-induced MR distortions. The first is to model the effect of

the materials in the patient. The second is to compare two images. Several studies of the first method have used *a priori* error fields [28]–[31]. Schmitt [32] used a two dimensional polynomial to describe a warping transformation of geometric distortion in phantom MR-scans; he ignored higher order terms. Yamamoto and Kohno's [33] phantom study used two gradients to correct both magnetic susceptibility error and gradient field nonlinearity.

Our approach to susceptibility error correction builds from the second method, comparison of pairs of MR images. Cho [34] proposed a method to correct susceptibility distortion using view angle tilting by adding a compensation gradient. Chang and Fitzpatrick [21] present a differential equation approach using warping transformation. This technique, used in several studies by the Vanderbilt group, assumes continuity of the image profile along the read-out direction, and that corresponding image features can be found in two serial slice by slice volume image acquisitions using different read-out gradients [4], [5], [21]. The success of this method greatly depends on the ability to properly establish point to point correspondence between the two image volumes. Additionally, this method appears prone to errors from image noise and line broadening. The latter is a result of the finite impulse response of MR scanners [22], [35]. A similar approach was taken in Moerland *et al.*'s frame-based study [25].

Sumanaweera [22] extensively tested a method that requires collecting a pair of images with identical scan parameters except for slightly differing echo recall times (TE). The off-resonant frequencies accrue additional phase [23] in the time interval ΔTE which enables generating a magnetic field inhomogeneity map from phase differences. Image distortions are corrected from the pixel shift information obtained from the map. The phase of the MR signal contains information about the geometric distortion caused by magnetic susceptibility. This fact has led to correction methods based on extraction of phase maps or B_0 maps from MR images [36].

Assumptions about differences in resonance are the basis of our volume MR susceptibility error correction strategy. The human body has two major constituents that generate MR signals: water and lipid. An MR spectrum showing a distribution of resonant frequencies of various compounds in an object shows that hydrogen atoms attached to water and fat molecules resonate at two distinct frequencies separated by about 205 Hz at 1.5 T [20]. Hence, at a first approximation, the MR spectrum can be thought off as two impulses in the frequency domain [22]. The MR spectrum $\rho(y, \omega)$ at location y is characterized by (1)

$$\rho(y, \omega) = \rho_\omega(y)\delta(\omega)m + \rho_f(y)\delta(\omega - \omega_f) \tag{1}$$

where $\rho_\omega(y)$ and $\rho_f(y)$ are the distributions of water and lipid respectively and ω_f is the chemical shift separation of lipid with respect to water. Proof of this model is in [22] and [23].

In practice, the phase of $(p(y, T + \Delta T))/(p(y, T))$ can be more than 2π. In this case aliasing occurs leading to phase wrapping. We use the phase unravelling method described in [20] to extract the correct phase. This algorithm carefully adds or subtracts multiples of 2π by tracking the trend of phase variation.

Ideally, a homogeneous magnetic field, B_0, is required throughout the image volume [23]. Due to the magnetic susceptibility of the object in the imaging space, the B_0 field is perturbed. The perturbations lead to off-resonant frequencies at each pixel $\Omega(y)$. These off-resonant frequencies acquire phase during a set time interval ΔT. Therefore, the phase accrued in ΔT can be used to determine the B_0 map. The pixel error map, which is identical to the B_0 map up to a known constant factor, determines the misregistration of the pixels in the image.

Our susceptibility error distortion correction algorithm generates a pixel position error profile from phase differences computed at each pixel location in two scans taken at a ΔT time interval. Here, P(TE) is the complex reconstructed image at TE, γ is gyromagnetic ratio, G_y is the frequency encoding gradient strength, and ΔT is the shift in TE time between the two acquisitions. Based on [19] and [22], and our knowledge of gradient linearity over the head's volume, we assume that the pixel shifts occur only in the frequency encoding (read out) direction as a result of object-induced magnetic susceptibility error. The pixel shift Δ_y at any position in an image is given by (2) as discussed in [22] and [23]

$$\Delta_y = \frac{\text{phase}\left\{\dfrac{P(\text{TE} + \Delta T)}{P(\text{TE})}\right\}}{\gamma G_y \Delta T}. \tag{2}$$

With the error profile determined, the correction can be effected by shifting the pixels to their correct locations followed by a linear interpolation and resampling of gray scale values. We compute error for only those pixels within the image volume above a determined pixel intensity threshold in order to eliminate contributions from background noise (e.g., random noise, static field inhomogeneity, etc.). Theoretically this algorithm can account for subpixel size shifts in pixel position. Unlike previous workers we compute an error map for correction by forward interpolation through the volume, a process referred to as "forward warping" [37]. Fractional contributions of gray levels from all neighboring pixels in the original image are determined for each pixel position in the corrected images. Gray scale values across the volume are interpolated and resampled to create corrected slice images.

V. Cadaver Phantom and Patient Study Methods

Sumanaweera *et al.* [24] have carefully tested their B_0 map correction of object-induced distortion with phantom (game hen), cadaver, and patient studies [6], [22], [24] in situations designed to model stereotactic neurosurgical operative procedures [6], [24]. We tested our geometric distortion correction protocol with three perfused cadaver phantoms and one live human subject. The cadaver heads were severed just below the humeral head and sternal angle, as a bust, and thereafter stored in sealed plastic bags to prevent dehydration. Prior to sealing the bags six IZI (plastic encased magnesium-chloride sponge) CT/MR skin-adhesive fiducial markers (Sophomor Danek, Memphis, TN) were sutured to the scalp (Fig. 1). The

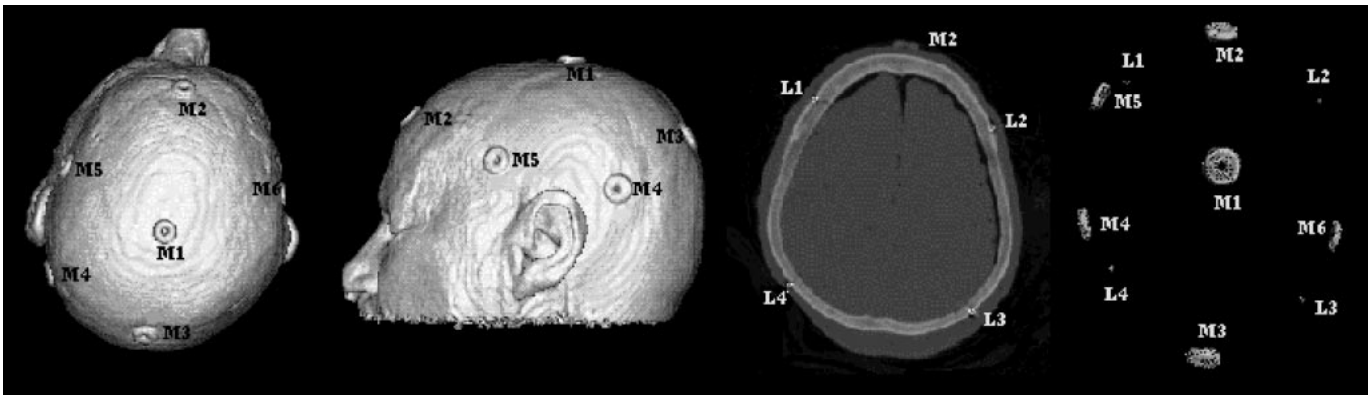

(a) (b) (c) (d)

Fig. 1. Stereotactic neurosurgical fiducial marker arrangement on cadaver head: 3D CT of cadaver head A (note: tip of nose was not in FOV, i.e., intentionally cut off). Markers M1–6 are shown in (a)–(c). The axial cut-away in (c) shows the four Beekley lead "spots" implanted firmly in the diploic space. (d) Shows the segmented fiducial marker volumes used to determine a centroid location. The CT/MR markers and lead spots were applied to roughly the same locations in all three cadaver heads.

IZI markers cross more than one slice, thus centroid location can be determined with sub voxel accuracy (cf. [4] and [5]). Three of the six IZI markers [Fig. 1(a)–(c)] were arrayed along the midsagittal plane at antero-superior, superior, and postero-superior positions, two laterally just antero-superior and postero-superior to the left ear, and the last anterior to the right ear. Next, four 1.5-mm lead Beekley (Bristol, CT) lead "spots" were implanted in the vault in a roughly quadrilateral formation [as indicated in Fig. 1(c)] where cortical bone had been chipped open. Caliper distances (0.01-mm gauge) were taken with the sharp needle tips overlying estimated lead ball centroids, the corresponding bone chip was replaced, and the overlying scalp sutured.

The cadaver heads were volume CT-scanned on a Siemens Somatom Plus IV as follows: 1 mm thick contiguous axial slices with 0° gantry tilt at an in-plane resolution of 512×512 pixels. The field of view (FOV) was chosen to be 225 mm, resulting in voxel dimensions of $0.44 \times 0.44 \times 1.0$ mm. The cadaver heads were also volume MR-scanned on a 1.5-T Siemens Magnetom Vision scanner. A FLASH3D sequence was used to obtain contiguous axial slices of 1-mm thickness with an in-plane resolution of 256×256 pixels, FOV of 225 mm leading to voxels of $0.89 \times 0.89 \times 1.0$ mm. Two acquisitions were made for each cadaver head with $G_y = 6.52$ mT/m, TR $= 10$ ms, tip angle $= 20°$. The TE's for the two acquisitions were chosen to be 4 and 8.4 ms with ΔTE $= 4.4$-ms data capture time was approximately 5.5 min. for each of the three cadaver heads. FOV and slice thickness parameters were chosen to obtain isotropic voxels in MR and CT. The CT images were reformatted to generate images of 256×256 resolution to match the MR image resolution. This creates voxels of identical dimensions in CT and MR thereby eliminating the need for anisotropic scaling of voxel dimensions during registration. However, it should be noted that Hill *et al.* [38] and Maurer *et al.* [5] have found that small scanner scaling calibration errors significantly affect image space localization and registration of widespread neurosurgical fiducial markers.

The IZI CT/MR fiducial markers were segmented from the CT and MR images using a region growing segmentation tool [39] and three dimentionally rendered using the "wrapper" [40] [Fig. 1(d)]. The four implanted lead spots were similarly identified in the 3D CT images. The 3-D coordinates of segmented marker centroids seen in CT, uncorrected MR, and corrected MR images were computed.

Finally, we collected two volume MR-scans of a live human subject to see whether the magnitude and areas of MR distortion error were similar to those in the cadaver data. The imaging protocol for the first MR-scan (patient A) was the same as that used for the cadaver study. The second MR-scan (patient B) of the same subject was acquired in 11 min. (additional time was required for whole head imaging) with increased FOV (256 mm), sagittal orientation, 256×256 pixels $\times 1.2$ mm. Both the A and B scans had $G_y = 6.52$ mT/m as in the cadaver study, thus pixel size is the most significant variant between the two live subject MR-scans. The B protocol approximates conventional MR-scans.

VI. Susceptibility Error Affect on Stereotactic Registration

The first step in our data analysis was to compare the caliper distances taken between the lead spots implanted in the cadaver heads and homologous computed distances in the 3D CT images. Measurement errors were less than 0.5 mm (Table I).

Next, the centroid coordinates of the fiducial markers, obtained from the cadaver 3D CT and 3D MR images were registered in Sofomor Danek's (Memphis, TN) ImMerge software. Separate x, y, and z direction, mean, maximum, and root mean square (rms) registration errors were obtained for each marker before and following susceptibility error-correction (Table II).

The maximum MR-to-CT fiducial centroid registration error was 2.69 mm and mean centroid registration error was 1.36 mm across all three uncorrected cadaver scans. The corrected fiducial centroid registration error maximum was 2.02 and mean centroid registration error was 1.09 mm across all three cadavers.

TABLE I
ERROR BETWEEN CALIPER MEASUREMENTS AND COMPUTED DISTANCES

Lead Spots	Cadaver A		Cadaver B		Cadaver C	
	Caliper	Computed	Caliper	Computed	Caliper	Computed
L1-L2	96.46	96.07	71.87	71.64	94.22	93.80
L2-L3	98.99	98.45	114.86	114.32	114.96	114.11
L3-L4	100.31	100.59	105.28	105.36	90.07	89.44
L1-L4	96.47	96.36	109.48	109.97	125.29	125.81

TABLE II
(a) REGISTRATION ERRORS OF UNCORRECTED CADAVER 3D MR TO 3D CT (VALUES IN MM). ED = EUCLIDEAN DISTANCE. A, B, AND C ARE THREE CADAVERS. X, Y, AND Z ARE THREE COORDINATES AT EACH FIDUCIAL MARKER, M1–6, AS SHOWN IN FIG. 1.
(b) REGISTRATION ERRORS OF SUSCEPTABILITY ERROR CORRECTED CADAVER 3D MR TO 3D CT. PARAMETERS ARE THE SAME AS IN (a)

	Ax	Ay	Az	ED	Bx	By	Bz	ED	Cx	Cy	Cz	ED
M1	0.60	0.40	0.50	0.88	-0.30	0.10	0.80	0.86	0.70	-0.70	2.50	2.69
M2	-0.10	0.80	0.40	0.90	-0.30	-1.70	0.90	1.95	-0.40	0.50	0.60	0.88
M3	0.20	-1.60	0.60	1.72	0.10	1.50	0.70	1.66	0.20	-1.00	-0.50	1.14
M4	-0.10	-0.50	-0.60	0.79	1.50	1.00	-0.90	2.01	-0.80	-0.70	-0.90	1.39
M5	-1.00	0.80	-0.40	1.34	0.60	-0.50	-0.80	1.12	-0.70	0.80	-0.70	1.27
M6	0.40	0.10	-0.60	0.73	-1.60	-0.40	-0.70	1.79	1.00	0.30	-0.90	1.38
MAX	0.60	0.80	0.60	1.72	1.50	1.50	0.90	2.01	1.00	0.80	2.50	2.69
MIN	-1.00	-1.60	-0.60	0.73	-1.60	-1.70	-0.90	0.86	-0.80	-1.00	-0.90	0.88
MEAN	0.40	0.70	0.52	1.06	0.73	0.87	0.80	1.56	0.63	0.67	1.02	1.46

(a)

	Ax	Ay	Az	ED	Bx	By	Bz	ED	Cx	Cy	Cz	ED
M1	0.07	-0.10	0.50	0.87	-0.40	0.10	0.60	0.73	0.70	0.60	1.80	2.02
M2	-0.10	-0.10	0.60	0.62	-0.30	-0.90	1.20	1.53	-0.10	0.00	0.30	0.32
M3	-0.20	-0.50	0.80	1.96	0.20	1.10	0.60	1.27	0.00	-0.40	-0.70	0.81
M4	0.10	-0.30	-0.40	0.51	0.60	0.60	-0.60	1.04	-0.20	-0.50	-0.80	0.96
M5	-0.60	0.70	-0.80	1.22	1.40	-0.50	-1.20	1.91	-0.40	0.40	-0.60	0.82
M6	0.10	0.30	-0.70	0.77	-1.50	-0.40	-0.60	1.66	0.40	0.70	-1.30	1.53
MAX	0.70	0.70	0.80	1.22	1.40	1.10	1.20	1.91	0.70	0.70	1.80	2.02
MIN	-0.60	-0.50	-0.80	0.51	-1.50	-0.90	-1.20	0.73	-0.40	-0.50	-1.30	0.32
MEAN	0.30	0.33	0.63	0.82	0.73	0.60	0.80	1.36	0.30	0.43	0.92	1.08

(b)

The root mean square MR-to-CT fiducial registration error improved by 17% following correction. Mean (across all three cadavers) registration error declined to 1.09 mm. Dropping one or two markers with poorest registration accuracy, further decreased mean fiducial registration error to 0.62 mm with an average maximum error of 0.93 mm. Fiducial marker inaccuracy may be due to marker or scalp compression or slippage. Registration error in the frequency encoding direction was reduced by 53% and improved up to 25% in the other two directions. A slight registration error increase at some markers along the z direction occurred following correction. The large pre-/post-correction x coordinate difference in cadaver C disappeared on removal of the noisiest fiducial marker centroid.

VII. SUSCEPTIBILITY ERROR DISTRIBUTION STUDY

Pixel error maps comparing the uncorrected and corrected cadaver image volumes resulted in an average maximum pixel shift error of 7.60 mm which was distributed equally, positively or negatively, in either read out direction across all three cadavers (Table III). A 3-D rendering of the error greater than 1 mm [23] confirms predictions that susceptibility error is concentrated at tissue interface regions (e.g., air/skin, air/mucosa, and scalp/skull) [22], [25]. Image distortion at the air/scalp interface is clearly seen as misregistration at the fiducial markers (Fig. 2). Errors are minimal deep within the relatively homogenous cadaver brains, however distortion is observed in the space around the cerebral ventricles where it

TABLE III
OVERALL ERROR STATISTICS FOR ALL FIVE 3D MR IMAGE VOLUMES IN THIS STUDY

	Mean μ_y		Std σ_y		Range	Max	
	+	-	+	-	(μ_y ! σ_y)	+	-
Cadaver A	0.62	-0.60	0.98	0.97	-1.58, 1.60	7.52	-7.59
Cadaver B	0.70	-0.68	1.09	1.06	-1.74, 1.79	7.57	-7.58
Cadaver C	0.60	-0.59	0.96	0.95	-1.54, 1.55	7.66	-7.66
Patient A	0.39	-0.39	0.62	0.70	-1.09, 1.01	7.55	-7.62
Patient B	0.76	-0.76	0.97	1.04	-1.80, 1.73	15.66	-15.53

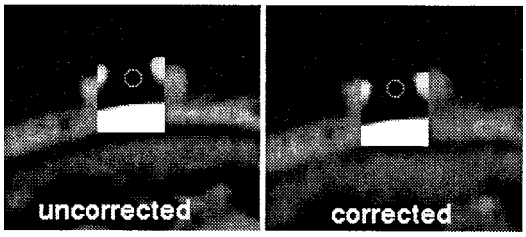

Fig. 2. Fiducial marker susceptibility distortion: CT/MR centroid overlay at one stereotactic fiducial marker. Considerable susceptibility error is found at the location of skin adhesive stereotactic fiducial markers, as elsewhere along the skin/air interface. Dramatic CT/MR fiducial-based co-registration improvement resulted following execution of our MR susceptibility distortion correction algorithm.

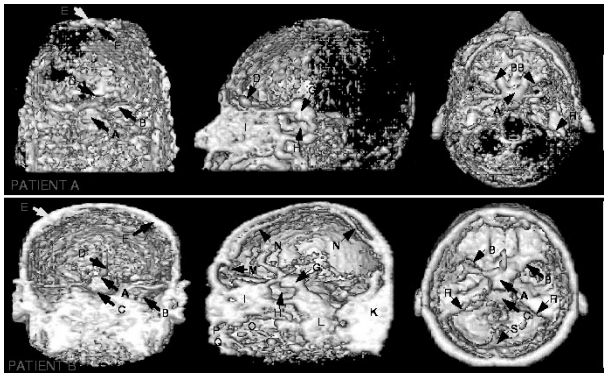

Fig. 3. Three-dimensional rendering of difference image between corrected and uncorrected 3D MR Images for two scans of the same patient. These are 3-D renderings of the susceptibility error greater than 1.0 mm. The patient A MR-scan protocol was the same high resolution MR-scan used in the cadaver study. The second MR-scan, patient B, was a similar scan protocol of the same person (i.e., patients A and B are the same person, the scan protocols are different) with 20% lower resolution (1.2 versus 1.0 mm), anisotropic pixels. Both images appear to display the scalp and mucosa interfaces with the air and with the skull. However, in the patient B MR-scan it appears that some of the bone-meninge interfaces also present high levels of susceptibility errors. Note: The coronal section is more posterior and the axial section more inferior in the patient B MR-scan. A: pituitary fossa, B: clinoid crest, C: sphenoid clivus, D: crista galli, E: scalp/air interface, F: scalp/skull interface, G: sphenoid body, H: sphenoid sinus, I: nasal septum, K: nuchal muscles, L: cervical vertebrae, M: frontal sinus, N: superior sagittal sinus, O: tongue, P: upper lip, Q: lower lip, R: petrous apex, S: confluence of sinuses.

appears air has leaked in. We also applied our susceptibility geometric distortion correction algorithm to two different MR-scans of the same subject. As noted, the first scan (patient A, Table III) was made with the cadaver study imaging protocol. The second scan (patient B, Table III) protocol (sagittal orientation, slice thickness 1.2 mm, FOV of 256 mm, 256×256 resolution) was more similar to common clinical protocols (i.e., lower resolution, thicker slice, shorter duration, and anisotropic voxels).

The patient A scan's mean pixel shift error was 0.39 mm with standard deviation of 0.66 mm. The patient B MR-scan presents mean pixel error of 0.76 with 0.98 mm standard deviation. Errors in negative and positive directions along the read-out axis (y) were nearly equal in both scans, with a -7.62 mm maximum in the A scan and 15.66-mm maximum in the B scan (Table III). The accuracy difference between scans A and B is due to voxel size.

Over the entire volume pixel shift errors were 37% less in patient scans A and B than in the cadaver study. However, cadaver and patient distortions are of similar magnitude at the skin surface, the scalp/skull interface, at the nasal mucosa, and at the skull base. A 3-D rendering (Fig. 3) of the error greater than or equal to pixel size (1 mm) presents significant error at the scalp/air and scalp/skull interfaces where frameless stereotactic fiducial markers are most commonly placed. The errors seen in the brain-meningeal (subarachnoid) interfaces and around the cerebral ventricles are not observed in the live patient error renderings.

VIII. CONCLUSIONS

Scanner-induced errors are now commonly corrected below pixel size by careful calibration and mathematical corrections. This is fortunate as our MR susceptibility correction algorithm is insensitive to remaining gradient field nonlinearity which is insignificant over the 225-mm FOV maximum used in this study. This validation of an algorithm for object-induced MR distortion correction differs from previous work done at Stanford [6], [22], [24], Vanderbilt [4], [5], [21], and Utrecht [25] in: 1) comparison of two live subject scans which suggest rapidly-acquired, high-resolution (small voxel dimensions), 3D MR images minimize pixel shift errors; 2) forward warping can carefully account for subpixel shifts during volume MR image correction; 3) a 3-D visualization of error distribution implicates large tissue interface surfaces; and 4) reliable image space determination of skin-adhesive fiducial marker centroids.

The results of this study suggest that real time object-induced susceptibility distortion correction could provide sub-pixel accuracy for frameless stereotactic neurosurgical procedures. Registration accuracy should improve with more regular marker shapes and centroid determination [41], [42]. Susceptibility error magnitude appears to be in proportion to

voxel dimensions. Our 3-D renderings of this error confirms susceptibility error concentration at tissue interfaces such as skin-air, scalp/skull, and mucosa-air, as predicted by [22] and [25]. The former two sites are the most common location for current frameless stereotactic neurosurgical fiducial markers.

ACKNOWLEDGMENT

The authors would like to thank Dr. R. Ratcheson, Chair, Department of Neurological Surgery, Case Western Reserve University (CWRU), Cleveland, OH, for providing funds to obtain the cadavers used in this study. They would also like to thank Dr. J. Haaga, Chair, Department of Radiology, CWRU, for providing gratis MR- and CT-scans for this project. They would like to thank T. Sumanaweera for providing his Ph.D. dissertation manuscript and E. Russell, Department of Radiology, CWRU, for performing the CT-scans. They would like to thank D. Lucien, Department of Biomedical Engineering, CWRU, for help in preparing the cadavers and assistance in calculating the accuracy of the CT data. Finally, they would like to thank the three anonymous reviewers for their comments.

REFERENCES

[1] R. Kikinis, P. L. Gleason, T. M. Moriarity, M. R. Moore, E. A. Alexander, III, P. E. Stieg, M. Matsumae, W. E. Lorensen, H. E. Cline, P. McL. Black, and F. A. Jolesz, "Computer-assisted interactive three-dimensional planning for neurosurgical procedures," *Neurosurg.*, vol. 38, pp. 640–651, 1996.

[2] J. Duquesnel, F. Turjman, M. Hermier, Y. Bascoulergue, A. Jouvet, G. Gervesy, and P. Tournut, "CT-guided needle biopsy of intra-cranial tumours: Results in 118 consecutive patients," *Acta Neurochir*, vol. [Suppl]63, pp. 16–19, 1995.

[3] K. J. Burchiel, T. T. Nguyen, B. D. Coombs, and J. Szumoski, "MRI distortion and stereotactic neurosurgery using the Cosman–Roberts–Wells and Leksell Frames," *Stereot. Funct. Neurosurg.*, vol. 66, pp. 123–136, 1996.

[4] R. J. Maciunas, J. M. Fitzpatrick, S. Gadamsetty, and C. R. Maurer, Jr., "A universal method for geometric correction of magnetic resonance images for stereotactic neurosurgery," *Stereotact. Funct. Neurosurg.*, vol. 66, pp. 137–140, 1996.

[5] C. R. Maurer, Jr., G. B. Aboutanos, B. M. Dawant, S. Gadamsetty, R. A. Margolin, R. J. Macunias, and M. J. Fitzpatrick, "Effect of geometrical distortion correction in MR on image registration accuracy," *J. Comput. Assist. Tomogr.*, vol. 20, pp. 666–679, 1996.

[6] T. S. Sumanaweera, G. Glover, P. F. Hemler, P. A. Elsen, D. Martin, J. R. Adler, and S. Napel, "MR geometric distortion correction for improved frame based stereotactic target localization accuracy," *Magn. Reson. Med.*, vol. 34, pp. 106–113, 1995.

[7] R. L. Galloway and R. J. Maciunas, "Stereotactic neurosurgery," *Crit. Rev. Biomed. Eng.*, vol. 18, pp. 207–233, 1990.

[8] L. Schad, S. Lott, F. Schmitt, V. Sturm, and W. J. Lorenz, "Correction of spatial distortions in MR imaging: A prerequisite for accurate stereotaxy," *J. Comput. Assist. Tomogr.*, vol. 11, pp. 499–505, 1987.

[9] D. Kondziolka and J. C. Flickinger, "Use of magnetic resonance imaging in stereotactic surgery," *Stereotact. Funct. Neurosurg.*, vol. 66, pp. 193–197, 1996.

[10] J. M. Taha, M. A. Lamba, C. Samaratunga, J. C. Beneman, and R. E. Warnick, "A method to reduce systematic spatial shift associated with magnetic resonance imaging," *Stereotact. Funct. Neurosurg.*, vol. 66, pp. 118–122, 1996.

[11] L. Walton, A. Hampshire, D. M. C. Forster, and A. A. Kemeny, "A phantom study to assess the accuracy of stereotactic localization, using T1-weighted magnetic resonance imaging with Leksell stereotactic system," *Neurosurg.*, vol. 38, pp. 170–178, 1996.

[12] E. Alexander III, H. M. Kooy, M. Van Herk, M. Schwartz, P. D. Barnes, N. Tarbell, R. V. Mulkern, E. J. Holupka, and J. S. Loeffler, "Magnetic resonance image-directed stereotactic neurosurgery: Use of image fusion with computerized tomography to enhance spatial accuracy," *J. Neurosurg.*, vol. 83, pp. 271–276, 1995.

[13] J. S. Gerdes, P. W. Hitchon, W. Neeranjun, and J. C. Torner, "Computed tomography versus magnetic resonance imaging in stereotactic localization," *Stereotact. Funct. Neurosurg.*, vol. 63, pp. 124–129, 1994.

[14] N. D. Kitchen, L. Lemieux, and D. G. T. Thomas, "Accuracy in frame-based and frameless stereotaxy," *Stereotact. Funct. Neurosurg.*, vol. 61, pp. 195–206, 1993.

[15] L. F. Czervionke, D. L. Daniels, F. W. Wherli, L. P. Mark, L. E. Hendrix, J. A. Strandt, A. L. Williams, and V. M. Haughton, "Magnetic susceptibility artifacts in gradient recalled echo MR imaging," *Amer. J. Neuroradiol.*, vol. 9, pp. 1149–1155, 1988.

[16] M. P. Heilbrun, B. M. Sunderland, P. R. McDonald, T. H. Wells, E. Cosman, and E. Cannes, "Brown–Roberts–Wells stereotactic frame modifications to accomplish magnetic resonance imaging guidance in three planes," *Appl. Neurophysiol.*, vol. 50, pp. 143–152, 1987.

[17] R. A. Meuli, F. R. Verdun, F. O. Bochud, L. Emsley, and H. Fankhauser, "Assessment of MR image deformation for stereotactic neurosurgery using a tagging sequence," *Amer. J. Neuroradiol.*, vol. 15, pp. 45–49, 1994.

[18] D. M. Dormont, D. M. Zerah, P. Cornu, F. Parker, B. Aubert, R. Sigal, J.-P. Francke, A. Zouaoui, and C. Marsaut, "A technique of measuring the precision of an MR-guided stereotaxic installation using anatomic specimens," *Amer. J. Neuroradiol.*, vol. 15, pp. 365–371, 1994.

[19] K. M. Ludeke, P. Roschmann, and R. Tischler, "Susceptibility artifacts in NMR imaging," *Magn. Reson. Imag.*, vol. 3, pp. 329–343, 1985.

[20] E. Schneider and G. Glover, "Rapid *in-vivo* shimming," *Magn. Reson. Med.*, vol. 18, pp. 335–347, 1991.

[21] H. Chang and J. M. Fitzpatrick, "A technique for accurate magnetic resonance imaging in the presence of field inhomogeneities," *IEEE Trans. Med. Imag.*, vol. 11, pp. 319–329, 1992.

[22] T. S. Sumanaweera, "Segmentation and distortion correction in medical imaging," Ph.D. dissertation, Stanford Univ., Stanford, CA, 1992.

[23] J. Kamath, "Correction of geometric distortion due to object-induced magnetic inhomogeneity in magnetic resonance images for use in stereotactic neurosurgery," M.Sc. thesis, Cleveland, OH, Case Western Reserve Univ., 1998.

[24] T. S. Sumanaweera, J. R. Adler, Jr., S. Napel, and G. H. Glover, "Characterization of spatial distortion in magnetic resonance imaging and its implications for stereotactic surgery," *Neurosurg.*, vol. 35, pp. 696–704, 1994.

[25] M. A. Moerland, R. Beersma, R. Bhagwandien, H. K. Wijrdeman, and C. J. Bakker, "Analysis and correction of geometric distortions in 1.5 T magnetic resonance images for use in radiotherapy treatment planning," *Phys. Med. Biol.*, vol. 40, 1651–1654, 1995.

[26] B. R. Rosen, V. J. Wedeen, and T. J. Brady, "Selective saturation NMR imaging," *J. Comput. Assist. Radiol.*, vol. 8, pp. 813–818, 1984.

[27] H. Rosenthal, K. R. Thulborn, D. I. Rosenthal, S. H. Kim, and B. R. Rosen, "Magnetic susceptibility effects of trabecular bone on magnetic resonance imaging of bone marrow," *Invest. Radiol.*, vol. 25, pp. 173–178, 1990.

[28] K. Sekihara, S. Matsui, and K. Kohno, "NMR imaging for magnets with large nonuniformities," *IEEE Trans. Med. Imge.*, vol. MI-4, pp. 193–199, 1985.

[29] K. Sekihara, M. Kuroda, and K. Kohno, "Image restoration from nonuniform magnetic field influence for direct Fourier NMR imaging," *Phys. Med. Biol.*, vol. 29, pp. 15–24, 1984.

[30] C. M. Lai "Reconstructing NMR images under magnetic fields with large inhomogeneities," *J. Phys. E Sci. Instrum.*, vol. 15, pp. 1093–1100, 1982.

[31] J. M. S. Hutchison, R. J. Sutherland, and J. R. Mallard, "NMR image recovery under magnetic fields with large nonuniformities," *J. Phys. E Sci. Instrum.*, vol. 11, pp. 217–221, 1978.

[32] F. Schmitt, "Correction of geometric distortion in MR-images," in *Proc. Int. Symp. CAR'85*, pp. 15–23.

[33] E. Yamamoto and H. Kohno, "Correction of distortion caused by field errors in MR imaging," *Soc. Magn. Res. Med.*, p. 402, 1987, (Abstracts).

[34] Z. H. Cho, D. J. Kim, and Y. K. Kim, "Total inhomogeneity correction including chemical shifts and susceptibility view angle tilting," *Med. Phys.*, vol. 15, pp. 7–11, 1988.

[35] A. Gauvin, "Geometric distortion of magnetic resonance images," Unpublished M.Sc. thesis, McGill Univ., Montreal, P.Q., Canada, 1992.

[36] E. Fieg, F. Greenleaf, and M. Perlin, "Magnetic resonance imaging with nonuniform fields," *Phys. Med. Biol.*, vol. 31, pp. 1091–1099, 1986.

[37] R. C. Gonzalez and R. E. Woods, *Digital Image Processing.* Reading, MA: Addison-Wesley, 1993.

[38] D. L. G. Hill, C. R. Maurer, Jr., C. Studholme, J. M. Fitzpatrick, and D. J. Hawkes, "Correcting scaling errors in tomographic images using a nine degree of freedom registration algorithm," *J. Comput. Assist. Tomogr.*, vol. 22, pp. 317–323, 1998.

[39] D. Dean, K. Subramanyan, J. Kamath, F. L. Bookstein, D. Wilson, D. Kwon, and P. Buckley, "Comparison of traditional brain segmentation tools with 3-D self-organizing maps," *Lecture Notes Comput. Sci.*, vol. 1230, pp. 393–398, 1997.

[40] A. Guéziec and D. Dean "The wrapper: A surface optimization algorithm that preserves highly curved areas," in *Proc. Visualization in Biomedical Computing 1994*, R. A. Robb, Ed., SPIE, Rochester, MN, 1994, vol. 2359-58, pp. 631–642.

[41] M. Y. Wang, C. R. Maurer, Jr., J. M. Fitzpatrick, and R. J. Maciunas, "An automatic technique for finding and localizing externally attached markers in CT and MR volume images of the head," *IEEE Trans. Biomed. Eng.*, vol. 43, pp. 627–637.

[42] M. Y. Wang, C. R. Maurer, Jr., and J. M. Fitzpatrick, "Partial volume effect on marker localization in medical density images," in *Proc. SPIE Conf. on Medical Imaging*, K. M. Hanson, Ed., SPIE, Newport Beach, CA, 1997, vol. 3034-55, pp. 580–591.